



Orbital-separation approach for consideration of finite electric bias within density-functional total-energy formalism

Shusuke Kasamatsu* and Satoshi Watanabe

Department of Materials Engineering, The University of Tokyo, 7-3-1 Hongo, Bunkyo-ku, Tokyo 113-8656, Japan

Seungwu Han†

Department of Materials Science and Engineering, Seoul National University, Seoul 151-742, Korea

(Received 7 May 2011; revised manuscript received 5 July 2011; published 23 August 2011)

We present a simple approach for the consideration of bias voltage within the Kohn-Sham formalism of density-functional theory. To be specific, the electronic charging of a metal-insulator-metal capacitor under bias voltage is considered explicitly. This is achieved by separating the Kohn-Sham orbitals around the Fermi level into anode or cathode parts and applying different Fermi levels in the determination of occupation numbers. The formal basis of the present approach is discussed in detail. We test this method against Au-vacuum-Au and Au-MgO-Au capacitors with various dielectric thicknesses. It is shown that the bulk optical and static dielectric constants can be obtained accurately. We also demonstrate that interface effects on capacitance can be investigated straightforwardly. Furthermore, we apply this method to the graphene capacitor and identify the quantum effects in the capacitance, which is well explained by the contribution of the kinetic energy of electrons to the capacitance. The present method can be readily implemented in conventional first-principles codes and provides a unified approach to evaluate capacitance of nanodevices.

DOI: [10.1103/PhysRevB.84.085120](https://doi.org/10.1103/PhysRevB.84.085120)

PACS number(s): 71.15.-m, 73.40.Rw, 77.22.-d

I. INTRODUCTION

Technological advances have made possible the fabrication and observation of electrical devices with characteristic lengths in the nanometer regime. Such devices sometimes exhibit unusual properties that can not be understood from classical physics. For example, metal-insulator-metal (MIM) capacitors with nanometer thickness (to be used, e.g., for next-generation DRAMs) sometimes exhibit capacitances that deviate significantly from what is expected from bulk measurements.¹⁻³ This is presumed to be due to the characteristics of the metal-insulator interface, the impact on the overall dielectric behavior of which becomes significant with increased interface to volume ratios in thin films. Therefore, it is crucial to understand the origin of such properties and to control them for achieving further scaling of nanodevices. Furthermore, it has been pointed out that the capacitance is comprised not only of the classical geometric capacitance, which is proportional to the inverse of the dielectric thickness, but also of contributions of quantum mechanical origin, which may become dominant as the dielectric thickness approaches the nanometer to subnanometer regime,⁴ or when low-dimensional materials such as carbon nanotubes and graphene are used.⁵⁻⁸

To clarify the origin of such nanoscale properties, one often resorts to quantum mechanical methods such as first-principles simulation based on the Kohn-Sham (KS) formalism of density-functional theory (DFT).^{9,10} However, conventional DFT methods can not account for bias voltage, which is essential in simulation of electrical devices. This is due to the fact that the original KS-DFT formalism seeks the global ground state with a unique Fermi level over the entire system. To overcome this limitation, several methods have been developed in recent years for consideration of bias voltage within the KS-DFT formalism.¹¹⁻²¹ However, they have not seen widespread use due to limitations in accuracy and/or efficiency, geometric constraints, and difficulty in implementation. We discuss some of these points in more detail below.

Quantum transport techniques such as nonequilibrium Green's function (NEGF) method,¹⁶ boundary-matching scattering-state density-functional method,^{13,14,22} and time-dependent DFT (Ref. 17) are each capable of describing the effect of finite electric bias, and they have been applied with success. However, these methods are still too costly in terms of computational power to apply to realistic systems, even on today's fastest computational facilities.

On the other hand, if we are concerned with insulating systems such as MIM capacitors, then we can resort to techniques that require much less computational resource. One way to deal with the situation is to consider a slab geometry and apply a sawtooth potential to simulate an external field.^{11,12} However, this does not work with MIM slabs because there is only one Fermi level in the system that is commonly applied to both metal slabs. In effect, the system would respond as if the metal parts were short circuited; the metal slabs would completely screen the electric field and the insulator part would not “feel” the bias at all. An alternative approach is to use metal-insulator (MI) slabs, as was demonstrated in Refs. 21 and 23. In this method, the capacitance of the MIM structure is calculated from the polarization and charge density difference profiles of the MI system under an external field. This has limitations, however, as insulator surfaces can be metallic, depending on the termination. Moreover, this method is limited in investigating quantum capacitance (see Sec. II A). An alternative to using a sawtooth potential is to modify the boundary condition in solving Poisson's equation to consider bias voltage, as is done in the effective screening medium method.¹⁸ However, this also does not escape from the same limitations due to the fact that the electronic states are filled according to a unique Fermi level.

Recently, it was shown that this problem can be resolved elegantly by introducing maximally localized Wannier functions (MLWFs) in considering the coupling of a periodic metal-insulator structure to an external field.^{20,24} This method

has been successful in examining dielectric dead layers at metal-insulator interfaces.^{25,26} However, since the field direction must be specified before the calculation, the method can practically deal with only parallel plate capacitors.

Another completely different approach for bias application has been proposed by Nakaoka *et al.*¹⁵ In the so-called partitioned real-space density-functional (PRDF) method, they consider two isolated electrodes with vacuum in-between. The KS equations for two electrode regions are solved independently, while Poisson's equation is solved for the entire system. This idea, however, can not be applied to MIM systems because the application of the method requires that there be no wave functions between the electrodes.

A similar idea, but one that avoids solving two KS equations, was proposed by Uchida *et al.*^{5,19} In this enforced Fermi energy difference (EFED) method, they consider the following free-energy functional:

$$\Omega = E[\rho] - \Delta\epsilon_F N[\rho], \quad (1)$$

where $E[\rho]$ is the KS energy of the capacitor with electronic density ρ , $\Delta\epsilon_F$ is the Fermi level difference between the electrodes, and $N[\rho]$ is the number of electrons transferred from anode to cathode by the battery. Solving the variational problem for Ω at constant $\Delta\epsilon_F$ leads to a set of slightly modified KS equations, which can be solved using the usual self-consistent iterations. Nevertheless, to define $N[\rho]$ unambiguously, all of the electrons must be confined to one of the electrodes; thus, this method can not be applied to MIM structures either.

In order to address the above-mentioned limitations in previous methods, we propose a very straightforward method that is based on separation of KS orbitals of the MIM system into anode and cathode parts. We will refer to this method as the orbital-separation approach (OSA) hereafter. In the OSA, the orbitals belonging to each electrode are occupied according to different Fermi levels, allowing for a fully self-consistent consideration of bias voltage in the limit of zero current between electrodes. An important characteristic of this method is that the total energy of the system is well defined, making possible the calculation of capacitance based on the energy-voltage relationship. Moreover, the numerical procedure is relatively simple and can be readily implemented in existing KS-DFT codes.

This paper is organized as follows. In Sec. II, we explain in detail about the OSA and its implementation into DFT codes. The theoretical basis for this method and its applicability to various situations are also discussed. In Sec. III, we present the calculation results for Au-vacuum-Au, Au-MgO-Au, and graphene-vacuum-graphene capacitors to demonstrate the robustness and accuracy of the present scheme. The summary and main conclusions will be provided in Sec. IV.

II. THEORETICAL BACKGROUND AND COMPUTATIONAL METHOD

A. Orbital-separation approach

In conventional self-consistent field (SCF) KS-DFT calculations utilizing the periodic boundary condition, the

lowest-energy KS orbitals are occupied in each SCF step leading to a single Fermi level in the entire system. The electron density is constructed as

$$\rho(\mathbf{r}) = \sum_{\mathbf{k}} \sum_i w_{\mathbf{k}} f_{\sigma}(\epsilon_{i,\mathbf{k}} - \epsilon_F) |\psi_{i,\mathbf{k}}(\mathbf{r})|^2, \quad (2)$$

where \mathbf{k} runs over sampled \mathbf{k} points in the Brillouin zone, i represents band indices, $w_{\mathbf{k}}$ is the \mathbf{k} -point weight, f_{σ} is the distribution function used for smearing of the occupation numbers (the magnitude of the smearing is controlled by the σ parameter), ϵ_F is the Fermi level, and $\psi_{i,\mathbf{k}}$ and $\epsilon_{i,\mathbf{k}}$ are orthonormalized KS orbitals and corresponding eigenenergies, respectively. The Fermi level ϵ_F is determined so that $\sum_{\mathbf{k}} \sum_i w_{\mathbf{k}} f_{\sigma}(\epsilon_{i,\mathbf{k}} - \epsilon_F) = N$, with N being the number of electrons in the supercell. In the OSA presented here, this occupation scheme is modified to simulate a system under bias voltage. In practice, we first obtain the ground-state electron density and KS orbitals using the conventional occupation scheme, then switch to the new scheme outlined below. Except for the occupation scheme, the SCF loops are carried out in the same manner as in conventional KS-DFT methods.

We consider a vacuum-metal-insulator-metal-vacuum capacitor structure as shown in Fig. 1(a). Dipole correction is applied in order to cancel the long-range dipole-dipole interaction between adjacent supercells in the direction perpendicular to the interface¹² (note that dipole correction formulas for the potential and the total energy given in Ref. 12 apply to any slab with a dipole, including the MIM system under finite bias voltage). To determine the occupation number of each KS orbital, we first determine the ground-state Fermi level in a specific SCF step following the conventional occupation scheme mentioned above. Then, we inspect the spatial distribution of each orbital within a preset energy window around the ground-state Fermi level [Fig. 1(b)]. The window has to be wide enough so that we can set the two new Fermi levels within that window, but it also has to be narrow enough so that the valence- and conduction-band states of the insulator are kept outside of the window. If the insulator is thick enough, there would be no orbital overlap between the electrodes, and the KS orbitals can be unambiguously separated into the right and left electrodes (the numerical criteria for separating the orbitals are discussed in the Appendix). This is actually a prerequisite for the application of this method (the condition of thick dielectrics will be elaborated on in Sec. IID). An exception is when two orbitals belonging to different electrodes are degenerate at the same \mathbf{k} point in the Brillouin zone. In this case, the wave function would exist in finite amounts on both electrodes. This is most significant when the two metal electrodes are symmetric. However, the degeneracy should be lifted at finite bias voltages owing to the asymmetric charge accumulation at the interfaces. At the initial stage, the degeneracy can be avoided by starting from the ground-state electron density under a small external electric field.

After separation, the orbitals within the window are occupied according to different Fermi levels, while the orbitals below this window are occupied fully and those above the window are left unoccupied. Specifically, the occupation

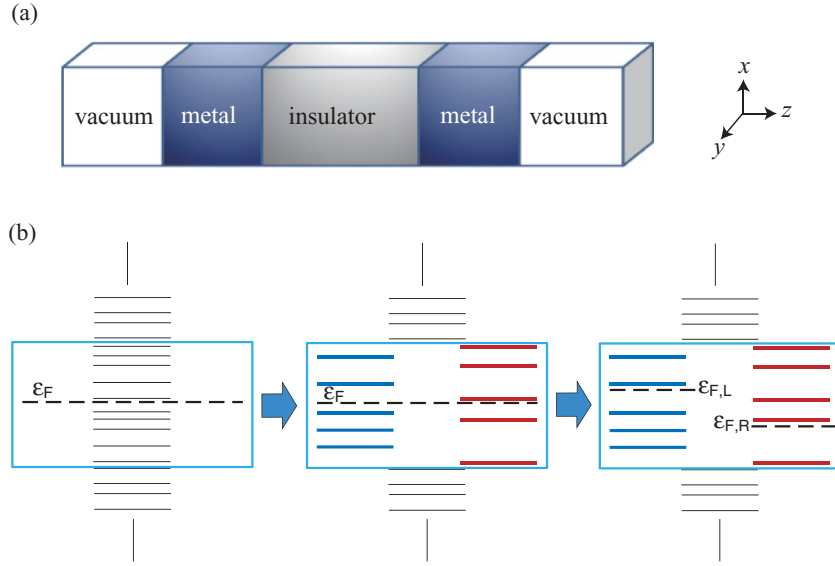


FIG. 1. (Color online) (a) Schematic of the simulation models considered in this work. The box indicates the boundaries of the periodic boundary condition employed in the calculations. (b) Schematic of the separation procedure within a preset window around the Fermi level.

functions are given as

$$f_i = \begin{cases} 1, & \epsilon_i < \epsilon_{\text{win}}^{\text{lower}} \\ 0, & \epsilon_i > \epsilon_{\text{win}}^{\text{upper}} \\ f_{\sigma}(\epsilon_{i,\mathbf{k}} - \epsilon_{F,L}), & i \in \text{window, L} \\ f_{\sigma}(\epsilon_{i,\mathbf{k}} - \epsilon_{F,R}), & i \in \text{window, R} \end{cases} \quad (3)$$

where $\epsilon_{\text{win}}^{\text{lower}}$ and $\epsilon_{\text{win}}^{\text{upper}}$ are the lower and upper bounds of the energy window, and L (R) stands for the orbitals separated into the left (right) electrode. The density $\rho(\mathbf{r})$ is then calculated according to the KS orbitals $\{\psi\}$ and the occupation functions $\{f\}$ in Eq. (3). The effective potential for the next SCF step is constructed based on this density. The external bias voltage V constrains the Fermi-level difference $\Delta\epsilon_F = \epsilon_{F,L} - \epsilon_{F,R}$ between the electrodes as follows:

$$\Delta\epsilon_F = eV, \quad (4)$$

where e is the electron charge. There is another condition that $\{f\}$ should satisfy:

$$\sum_{\mathbf{k}} \sum_i w_{\mathbf{k}} f_i = N, \quad (5)$$

where N is the number of electrons within the supercell. The Fermi levels $\epsilon_{F,L}$ and $\epsilon_{F,R}$ are determined by Eqs. (3)–(5).

The total free energy of the ion-electron system is written in the same manner as in the conventional KS scheme with the occupation functions $\{f\}$ and density $\rho(\mathbf{r})$ constructed according to the prescription detailed above:

$$\begin{aligned} F_{\text{cap}}^{\text{KS}}[\{\psi\}, \{f\}, \{\mathbf{R}\}] &= \sum_i f_i \langle \psi_i | \hat{T} + \hat{V}_{\text{NL}}^{\text{ion}} | \psi_i \rangle + E_{\text{H}}[\rho] \\ &+ E_{\text{xc}}[\rho] + \int d^3\mathbf{r} \hat{V}_{\text{loc}}^{\text{ion}}(\mathbf{r}) \rho(\mathbf{r}) \\ &+ E_{\text{II}}(\{\mathbf{R}\}) - \sum_i \sigma S(f_i). \end{aligned} \quad (6)$$

In Eq. (6), \hat{T} is the kinetic energy operator, $\hat{V}_{\text{NL}}^{\text{ion}}$ is the nonlocal part of the ionic pseudopotential, E_{H} is the Hartree energy, E_{xc} is the exchange-correlation energy functional, $\hat{V}_{\text{loc}}^{\text{ion}}$ is the local part of the pseudopotential, E_{II} is the Madelung energy of the

ions, and the last term is the entropy term that arises from the partial occupancies f_i .²⁷ Note that the summation in \mathbf{k} points has been omitted from Eq. (6) to simplify the notation.

It is worth mentioning that the present method controls the Fermi-level difference eV between electrodes; this does not necessarily correspond to the electrostatic (Hartree) potential difference.⁴ This is especially true when utilizing low-dimensional electrodes, the total capacitance of which includes a significant contribution from the quantum capacitance. However, if the metal slab is thick enough, the electronic band structure in the middle of the metal slab should be the same as in bulk due to the complete screening in the interfacial region. Since the Fermi level in bulk is fixed with respect to the band structure, and the band structure is referred to the electrostatic potential, the Fermi-level difference between electrodes would correspond to the electrostatic potential difference.

We point out that the OSA can be understood as an extension of the Δ SCF method used to calculate excited states of molecules.^{28,29} In the Δ SCF method, electron-hole pairs are introduced by transferring an electron from an occupied KS orbital to an unoccupied one. The KS effective potential is constructed from this excited electronic density, and the usual SCF procedure is carried out while keeping the hole in the specific orbital. Although this method appears to be at odds with the original KS formalism, a formal basis was put forward in Ref. 30 in which the Δ SCF method is shown to be an approximation of an exact excited-state KS formalism.

B. Variational nature and forces

In order to examine the variational nature of the OSA and to derive an expression for the forces, we consider the total free energy (Ω) of a capacitor connected to an external battery with voltage V :

$$\Omega = E_{\text{cap}}^{\text{QM}}[\Psi, \{\mathbf{R}\}] - VQ, \quad (7)$$

where $E_{\text{cap}}^{\text{QM}}$ is the quantum mechanical energy of the capacitor with electrons represented by the many-body wave function Ψ and ions fixed at positions $\{\mathbf{R}\}$, and $-VQ$ corresponds to the chemical energy of the battery. Q is the charge moved

from cathode to anode, which can be precisely measured in experiment by inserting an ammeter into the circuit. At equilibrium, the free energy Ω is minimized at $Q = Q_0$ and $\Psi = \Psi_0$. We set $E_{\text{cap}}^{\text{QM}}[\Psi_0, \{\mathbf{R}\}]$ as E_0 . The equilibrium condition also requires that the local Fermi levels of the two electrodes differ by eV . Suppose that the external battery is instantly removed after equilibrium is reached. The capacitor is now isolated, but the many-body wave function and hence $E_{\text{cap}}^{\text{QM}}$ should remain the same (Ψ_0 and E_0 , respectively). This means that E_0 is the minimum energy of the capacitor under the constraints that either (i) Fermi levels of the two electrodes differ by eV or (ii) the charge transfer between electrodes is Q_0 . These two constraints are equivalent since Q_0 monotonically depends on V for given atomic positions (except for regions where the capacitance is negative). The second constraint on Q_0 is tricky to impose in the presence of a dielectric layer because it is nontrivial (if not impossible) to separate the free charge (Q) and the polarization charge from the total charge density; thus, we utilize the first constraint. In short, we recast the problem into finding the minimum energy state of the capacitor under the constraint of a specific Fermi-level difference between electrodes. In this paper, $E_{\text{cap}}^{\text{QM}}$ is replaced by the KS free-energy functional ($F_{\text{cap}}^{\text{KS}}$) in Eq. (6), and the local Fermi level is controlled by the OSA mentioned in the preceding section. Since we seek the minimum KS energy under a certain constraint on orbital occupation, the KS equation can be employed in the same manner as in conventional density-functional calculations as long as the local Fermi level is adjusted at each iteration step.

One can obtain the change in Ω when an atomic coordinate shifts from R to $R + dR$ by following a two-step procedure: first, the circuit is opened and the ion moves by dR with the current flow prohibited and the charge transfer Q fixed. Then, the change in the free energy is limited only within the capacitor part such that $d\Omega_1 = (\partial F_{\text{cap}}^{\text{KS}}/\partial R)_Q$. Concurrently, the voltage between electrodes increases by dV . Second, the circuit is connected to the battery and the extra charge transfer dQ occurs to negate the voltage change. The battery lowers the free energy by $-VdQ$, while $F_{\text{cap}}^{\text{KS}}$ increases by

$$dF_{\text{cap}}^{\text{KS}} = (\epsilon_{F,L} - \epsilon_{F,R})dQ/e = VdQ \quad (8)$$

(according to Janak's theorem³¹). These terms cancel, so there is no change in the free energy in the second step ($d\Omega_2 = 0$). Therefore,

$$(d\Omega)_V = \left(\frac{\partial F_{\text{cap}}^{\text{KS}}}{\partial R} \right)_Q dR, \quad (9)$$

and thus the force acting on the atom can be calculated as

$$f_V = -\left(\frac{\partial \Omega}{\partial R} \right)_V = -\left(\frac{\partial F_{\text{cap}}^{\text{KS}}}{\partial R} \right)_Q. \quad (10)$$

In fact, this is exactly the one obtained by Hellmann-Feynman theorem within the KS formalism since it is calculated, in principle, under the assumption that the occupation numbers do not change and hence Q is kept constant. Thus, the forces (including Pulay corrections) can be calculated in the same manner as in the conventional KS scheme (see, e.g., Refs. 32–34). This means that the only part that needs modification in

conventional KS-DFT codes is the determination of the occupation numbers $\{f\}$. The other parts (e.g., forces and energies) are calculated from $\{f\}$ in the same manner as in the ground-state scheme.

C. Evaluation of capacitance from the total energy

As a final step, we elaborate on how to calculate the capacitance (C). We start with the fundamental definition of capacitance density as follows:

$$\frac{C(V)}{A} = \frac{1}{A} \frac{dQ}{dV}, \quad (11)$$

where dQ is the charge transferred between electrodes when the voltage changes from V to $V + dV$, and A is the surface area of the capacitor. As mentioned earlier, in applying Eq. (11) within the first-principles framework, it is difficult to distinguish the free charge and polarization charge in the total charge if there is a dielectric media between the electrodes. Instead, we utilize the total energy in the following way: the energy increase ($dF_{\text{cap}}^{\text{KS}}$) by moving dQ is given by VdQ [see Eq. (8)]. Inserting this into Eq. (11) results in the following formula of capacitance density in terms of the total energy:

$$\frac{C}{A} = \frac{1}{AV} \frac{dF_{\text{cap}}^{\text{KS}}}{dV}. \quad (12)$$

D. Applicability of our method

Our idea of separating the KS orbitals into two electrodes is similar to the PRDF (Ref. 15) and EFED (Refs. 5 and 19) methods mentioned earlier. However, the present method surpasses them by providing far more freedom in the system geometries that can be calculated. That is, while the PRDF and EFED methods require that the orbitals in the electrode regions are completely isolated from each other throughout all occupied states, this method can be used as long as the orbitals *around the Fermi level* are well separated.

We also note that the present scheme is compatible with any basis expansion method (plane wave, localized orbitals, augmented plane wave, etc.) as long as eigenfunctions and eigenvalues are obtained in the calculation. It should be possible even to apply to the Hartree-Fock method.

It is noted that the present method fixes the bias voltage V between the electrodes. That is, there is no external field, but, rather, an external battery. Thus, our situation can be interpreted straightforwardly as a finite object (i.e., a single capacitor) connected to a battery. Due to this closed-circuit condition, the total energy of the capacitor is not a conserved quantity as the external battery can do work on the system. On the other hand, the open-circuit condition can be simulated when there is a vacuum region between the electrodes. In this case, all electrons can be counted as belonging to either side of the vacuum, and fixing the amount of charge in each side allows one to simulate the open-circuit situation. The energy should conserve in this case. We note that the MLWF approach can handle both open- and closed-circuit situations even in the presence of dielectrics by fixing the electric displacement or the electric field.²⁴

The important prerequisite for using our method is that electronic states from different electrodes do not overlap

meaningfully inside the dielectrics. This is the case as long as the dielectric is thicker than 1 nm. For dielectric layers thinner than this, the direct tunneling currents would be so significant that it would not function as a well-defined capacitor. Therefore, the present method can be employed in most practical applications.

Another limitation of the present method is that, unlike quantum transport techniques such as NEGF-based methods, it can not consider electronic current between electrodes. However, while the implementation of the NEGF method is practically limited to localized basis sets, the OSA can be used for any basis set (including plane waves). This means that, in the limit of zero current, our method may give a much more accurate description of the self-consistent electronic structure under applied bias voltage. Thus, the charge density and ionic positions from the present method can serve as a good approximation in the limit of small current density. Furthermore, unlike the NEGF method where semi-infinite electrodes can be considered, our method requires that the electrode is finite in at least one direction. This may seem like a disadvantage, but, in fact, this system setup leads to a well-defined total energy of the system under bias voltage. This is an obvious advantage over NEGF-based methods, where the total energy of the system has not been defined unambiguously. Moreover, this setup allows for the calculation of nanoelectrodes, e.g., monolayer metals and graphene as will be demonstrated in the next section.

III. APPLICATION AND NUMERICAL TESTS ON NANOCAPACITORS

It is rather straightforward to implement the OSA in existing DFT codes since the only part that needs modification is the determination of the occupation number for each orbital. In this work, we implemented this method in Vienna *ab initio* simulation package^{33,34} (VASP) and performed calculations on Au(100)-vacuum-Au(100) and Au(100)-MgO(100)-Au(100) nanocapacitors of several dielectric thicknesses. A 6×6 Monkhorst-Pack \mathbf{k} -point mesh was used in the interface parallel directions, with a single Γ -point sampling in the perpendicular direction. We also performed calculations on a graphene-vacuum-graphene capacitor employing a $161 \times 161 \mathbf{k}$ -point mesh (the reason for such dense sampling will be discussed later). The Gaussian smearing method was used with a smearing width of 0.05 eV. The projector augmented wave method^{35,36} was used for treating electron-ion interactions, and a cutoff energy of 500 eV was used for the expansion of the KS orbitals using a plane-wave basis set. The local density approximation^{37,38} (LDA) was employed for the exchange-correlation functional. Dipole correction¹² as implemented in VASP was used to cancel the dipole-dipole interaction between adjacent unit cells. The total energies were converged within 10^{-8} eV per supercell. When performing structural relaxation, the force on each atom was converged within 0.001 eV/Å. We note that these are relatively strict criteria for convergence, but they are necessary to address the small energy changes under bias voltage. However, since convergence is usually exponential, this should not pose a big problem for most cases with the appropriate choice of calculation parameters.

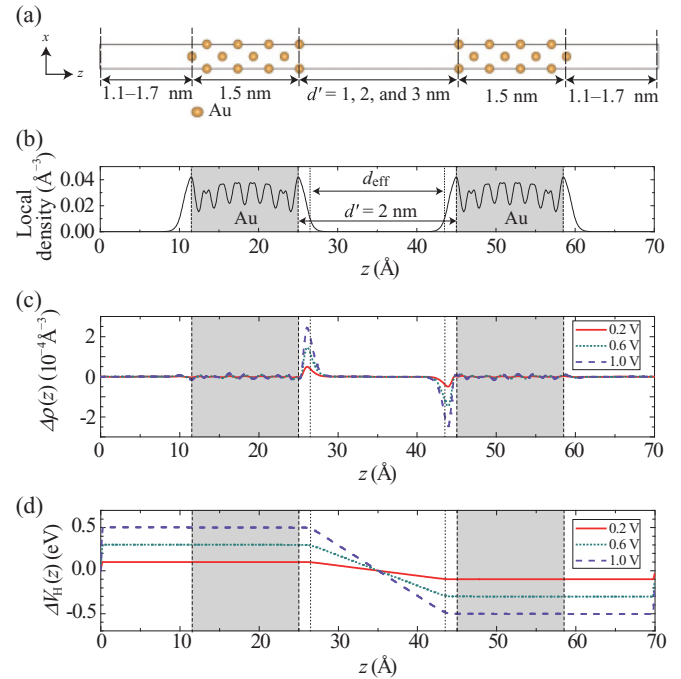


FIG. 2. (Color online) (a) The Au-vacuum-Au capacitor model used in this work. The box represents the periodic boundary condition. (b) xy -plane average of the electron density obtained by integrating the states between ± 1 eV around the Fermi level under zero bias, (c) xy -plane average of the induced charge density at various bias voltages, and (d) xy -plane average of the electrostatic potential difference (ΔV_H) with respect to zero bias results. In (b)–(d), the results for $d' = 2$ nm are presented. The vertical dashed lines indicate the position of the surface Au nuclei, while the dotted lines indicate the position of the surface corresponding to the effective vacuum thickness d_{eff} (see text).

A. Au-vacuum-Au capacitor

We first examine the effect of bias voltage on the system shown in Fig. 2(a). The capacitor is comprised of two Au electrodes sandwiching vacuum, and each electrode is comprised of 8 Au(100) layers. Figure 2(b) shows the xy average of the electron density corresponding to the states near the Fermi level. It can be seen that the prerequisite of having no orbital overlap between the electrodes is well satisfied.

We calculate the plane-averaged induced charge [$\Delta\rho(z)$] due to applied bias as follows:

$$\Delta\rho(z) = \frac{1}{L_x L_y} \int_0^{L_x} dx \int_0^{L_y} dy [\rho(x, y, z; V) - \rho(x, y, z; 0)], \quad (13)$$

where $\rho(x, y, z; V)$ is the charge density at position (x, y, z) under bias voltage V , and L_x (L_y) is the dimension along the x (y) direction. Most of the induced charge is confined within ~ 5 Å from the surface [Fig. 2(c)]. The change in the electrostatic potential [$\Delta V_H(z)$] due to bias application is calculated in the same manner:

$$\Delta V_H(z) = \frac{1}{L_x L_y} \int_0^{L_x} dx \int_0^{L_y} dy \times [V_H(x, y, z; V) - V_H(x, y, z; 0)], \quad (14)$$

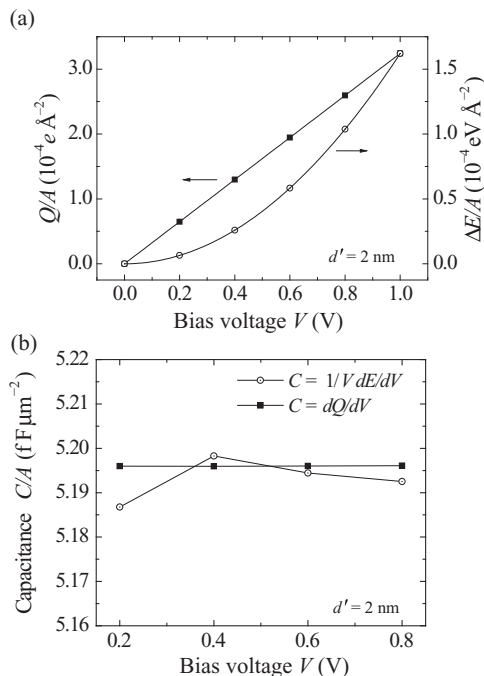


FIG. 3. (a) The accumulated surface charge density (left y axis) and total energy change (right y axis) as functions of bias voltage. (b) The capacitance evaluated from the total energy (open circle) and from the accumulated charge (solid square). The results are presented for the Au-vacuum-Au capacitor with a vacuum thickness of $d' = 2 \text{ nm}$.

where $V_H(x, y, z; V)$ is the local electrostatic potential at position (x, y, z) under an applied bias voltage V . As shown in Fig. 2(d), $\Delta V_H(z)$ is flat in the metal electrodes and drops linearly in the vacuum region as expected from elementary electrostatics. The potential difference between the two electrodes corresponds almost exactly (within 1%) to the applied Fermi-level difference eV .

Figure 3(a) shows the total energy and total accumulated surface charge as a function of bias voltage. The total energy with respect to zero bias $\Delta E = F_{\text{cap}}^{\text{KS}}(V) - F_{\text{cap}}^{\text{KS}}(0)$ is a parabolic function of voltage as expected from classical electrostatics ($E = 1/2CV^2$). The accumulated charge Q is linear with respect to voltage, and this is also the expected behavior ($Q = CV$). In Fig. 3(b), the capacitances evaluated from Eqs. (11) and (12) using central differences are shown and it is seen that they agree within 0.2%. This strongly suggests that Eq. (12) produces reliable capacitance values.

Next, we examine the dependence of the capacitance on the vacuum thickness. Classically, the capacitance can be written as a function of vacuum thickness d as $C = \epsilon A/d$. However, when performing atomistic calculations, d can not be defined unambiguously due to the spill-out of electrons into the vacuum as can be seen in Fig. 2(c). Here, we assume that the effective vacuum thickness d_{eff} differs by a constant from the distance between the surface atoms facing each other (d'). That is to say, the inverse capacitance can be written as

$$\frac{A}{C} = \frac{d_{\text{eff}}}{\epsilon} = \frac{d' - \Delta}{\epsilon}. \quad (15)$$

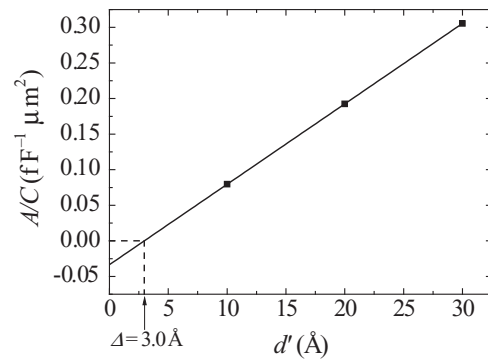


FIG. 4. The inverse capacitance of the Au-vacuum-Au capacitor with respect to d' .

Figure 4 shows the calculated inverse capacitance as a function of d' . We performed a linear fit of the data and confirmed that the slope equals the inverse of the vacuum permittivity (the error was within 0.02%). From the x intercept, Δ is evaluated to be 3.0 \AA . The position of this “effective surface” is shown in Figs. 2(b)–2(d) with dotted lines (we have assumed that $\Delta/2$ is assigned equally to both surfaces). The effective surface coincides well with the boundary from which the electrostatic potential drops linearly. It should be noted that the Δ value includes the effect of the spill-out of electrons into the vacuum as well as the effect of the quantum capacitance,²² although the latter would be small due to the relatively large density of states (DOS) of Au electrodes around the Fermi level.

B. Au-MgO-Au capacitor

As a more realistic example, we consider the Au-MgO-Au capacitor model as in Fig. 5(a). A thin film of MgO is sandwiched between two 8-layer Au electrodes. The z direction corresponds to the (100) orientation of MgO and Au. Figure 5(b) shows the electron density corresponding to the states around the Fermi level. One noticeable feature that is distinct from the vacuum capacitor is the development of metal-induced gap states (MIGs) at the edge of the dielectric. Nevertheless, the orbitals of the two metal plates around the Fermi level have no overlap (within numerical accuracy) with each other, so the OSA is applicable to this system as well. The band gap of the dielectric limits the amount of bias voltage that can be applied, but this is not an issue in this work since the bias voltage is increased only up to 1 V.

The change in the electrostatic potential (ΔV_H) due to bias application is shown in Fig. 5(c) with the atomic structure fixed or relaxed. When the structure is fixed, ΔV_H is similar to that of the vacuum capacitor [Fig. 2(d)]: the potential is flat in the electrodes and drops linearly inside the insulator film. When the structure is relaxed, on the other hand, atomic-scale oscillations occur due to the small movement of the ions, but the same amount of potential difference is maintained between the electrodes.

The voltage-energy relation of the Au-MgO-Au capacitor with 9 MgO(100) layers is shown in Fig. 6(a). Again, the total energy is a parabolic function of bias voltage as in the vacuum capacitor. The relaxed systems have higher energies than the fixed systems at the same voltage, and this might seem strange at first sight. However, this is actually the

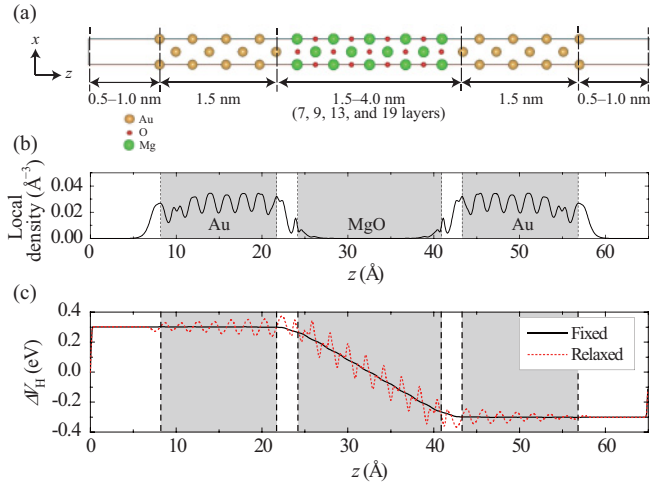


FIG. 5. (Color online) (a) Schematic of the Au-MgO-Au capacitor model under study, (b) xy -plane average of the electron density obtained by integrating the states between ± 1 eV around the Fermi level under zero bias, and (c) xy -plane average of the electrostatic potential with respect to that at zero bias. The results are given for the capacitor with 9 MgO layers whose structure was fixed (solid line) or relaxed (dashed line) at $V = 0.6$ V. The vertical dashed lines indicate the positions of the surface nuclei.

expected behavior because dielectric relaxation allows for further charging of the capacitor, and the total free energy including the chemical energy of the battery decreases (see Sec. II B). From this voltage-energy curve, the capacitance at each voltage is evaluated by Eq. (12) using central differences, and the results are plotted in Fig. 6(b) [we recall that Eq. (11) can not be used when there is a dielectric]. It is seen that the capacitance is almost constant with respect to voltage, meaning that the voltage dependence is almost negligible. This is consistent with the fact that the calculated voltage-energy curve is almost perfectly parabolic, following the classical relation $E = 1/2CV^2$ for voltage-independent capacitance.

Next, we look at the dependence of the capacitance on dielectric thickness. For the sake of analysis, we divide the dielectric into bulk and interfacial parts and rewrite the total capacitance as

$$\begin{aligned} \frac{A}{C_{\text{tot}}} &= A \left(\frac{1}{C_i} + \frac{1}{C_b} + \frac{1}{C_i} \right) \\ &= \frac{1}{\epsilon_0} \left[2d_i \left(\frac{1}{\epsilon_i} - \frac{1}{\epsilon_b} \right) + \frac{d}{\epsilon_b} \right], \end{aligned} \quad (16)$$

where A is the area of the capacitor plates, C_i and C_b are interfacial and bulk capacitances, ϵ_0 is the permittivity of vacuum, ϵ_i and ϵ_b are the interfacial and bulk dielectric constants, d is the nominal thickness of the dielectric, and d_i is the thickness of the interfacial part. The nominal thickness is defined by the number of layers multiplied by the interlayer distance in bulk. By plotting the inverse capacitance as a function of the dielectric thickness and fitting it to Eq. (16), one can evaluate ϵ_b from the slope. We can also see if there is indeed an ‘‘interfacial part’’ by examining the intercept.

Figure 7 shows the inverse capacitance at 0.6 V plotted against various dielectric thicknesses. They are fitted very well with a linear function, suggesting that the above fitting

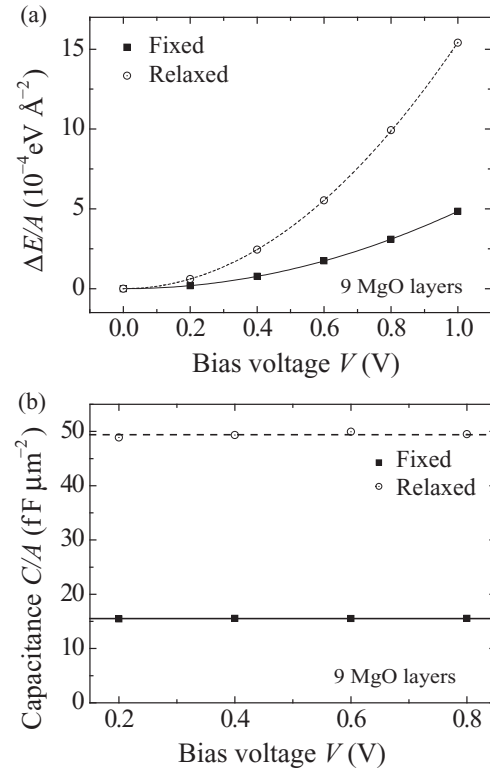


FIG. 6. (a) The total energy with respect to that at zero bias and (b) capacitance as functions of bias voltage. The results are given for the capacitor with 9 MgO layers whose structure was fixed at the zero bias structure (solid squares) and that relaxed at each bias voltage (open circles).

equation captures the essential physics of the system. From the slope for the fixed system, we obtained the bulk optical (ion-clamped) dielectric constant of 3.18. We also performed the same analysis on the relaxed system, and obtained a bulk static dielectric constant of 9.53.

To assess the accuracy of this result, we calculated the bulk optical and static dielectric constants using density-functional perturbation theory. The calculations were performed on the unit cell with one formula unit of MgO employing a $6 \times 6 \times 6$ Γ -centered \mathbf{k} -point mesh. The computed optical and

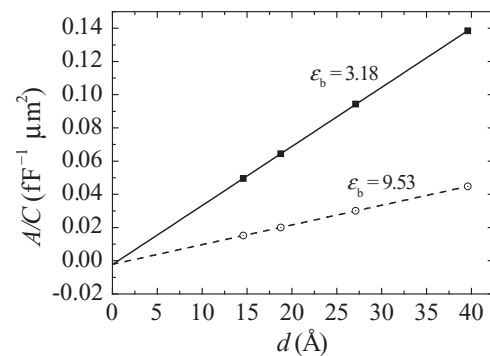


FIG. 7. Inverse capacitances of the Au-MgO-Au capacitor under bias voltage of 0.6 V are plotted with respect to the nominal dielectric thickness for fixed (solid squares) and relaxed (open circles) conditions.

static dielectric constants are 3.18 and 9.59, respectively. These values are in almost perfect agreement with our analysis of the interface system, which indicates that the energies and forces calculated from this method are reliable.

The negative y -axis intercept in Fig. 7 suggests the existence of a negative dead layer,²⁶ i.e., the capacitance including interface effects is slightly larger than that expected from the bulk dielectric constant. This agrees with previous theoretical works on the Ag-MgO-Ag^{7,20} and Au-MgO-Au^{8,21} systems, which calculated the capacitance from polarization induced by a constant external electric field.

C. Monolayer electrodes

An advantage of the OSA is that the treatment of nanoelectrodes is relatively straightforward. To demonstrate this, we performed calculations on MgO capacitors with monolayer Au electrodes shown in Fig. 8(a). The electron density corresponding to the states around the Fermi level is shown in Fig. 8(b), and it is seen that there is no orbital overlap between the two electrodes. The change in the electrostatic potential due to bias application [Fig. 8(c)] is very similar to that of the 8-layer electrode system when the structure is fixed. On the contrary, when the structure is relaxed, a large dipole is seen at the position of the monolayer electrodes. However, the electrostatic potential difference between the electrodes is still almost the same as the applied bias voltage. This shows that even a monolayer of Au can act as a nearly perfect screening medium. We also examined the dependence of the inverse capacitance on the dielectric thickness (Fig. 9). The slope is identical to that of the 8-layer electrode system, but the y intercept is slightly lower. This indicates that the capacitance is slightly larger than the 8-layer system. This is possibly due to the change in the interaction between the electrode and the dielectric as a function of electrode thickness. The

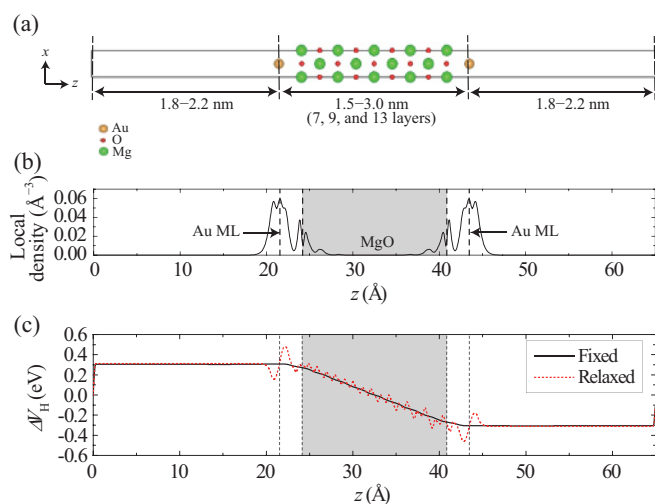


FIG. 8. (Color online) (a) Schematic of the MgO capacitor with monolayer Au electrodes, (b) electron density corresponding to the states at ± 1 eV around the Fermi level under zero bias, and (c) the xy -plane average of the change in the electrostatic potential due to bias application for fixed (solid line) and relaxed (dashed line) structures.

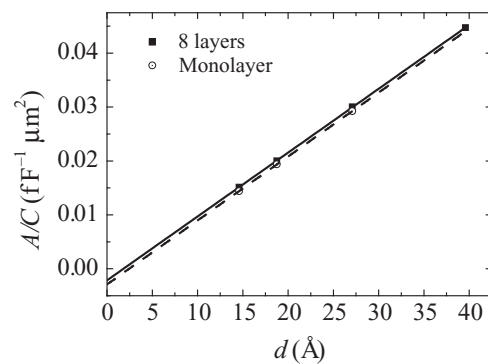


FIG. 9. Comparison of the inverse capacitance of MgO capacitors with 8-layer (solid squares) and monolayer (open circles) Au electrodes.

difference is subtle, however, and we do not have any concrete results that clarify the mechanism for this behavior.

D. Quantum capacitance of graphene electrodes

As mentioned earlier, the total capacitance is comprised of the classical geometric capacitance ($\propto \epsilon/d$) as well as quantum corrections arising from the kinetic, exchange-correlation, and electron-phonon interaction energies in the total-energy functional.⁴ Here, we investigate the applicability of our method for studying such effects using graphene-vacuum-graphene capacitor as an example. It has been pointed out that the quantum capacitance of graphene would become comparable to the classical geometric capacitance when using nanometer-thickness dielectrics. This is due to the band structure of graphene, which has a linear dispersion with vanishing DOS at the Fermi level. Fang *et al.* derived the kinetic term for $k_b T \ll eV_{ch}$ as

$$\frac{C_{kin}}{A} \simeq e^2 \frac{2}{\pi} \frac{eV_{ch}}{(\hbar v_F)^2}, \quad (17)$$

where V_{ch} is the channel potential and v_F is the Fermi velocity⁷ (they refer to this term as the quantum capacitance). eV_{ch} is the displacement of the Fermi level due to the charging of the graphene sheet. If we consider only the kinetic term as quantum corrections, then the total capacitance can be written as a series capacitor comprising of the geometric capacitance C_{geo} and the kinetic capacitance C_{kin} coming from the two graphene electrodes. This results in the following total capacitance density as a function of bias voltage:

$$\frac{C}{A} = \frac{e}{A} \frac{dn}{dV} = \frac{C_{geo}}{A} \left[1 - \left(1 + \frac{1}{2} \frac{n_{geo}}{n_{kin}} \right)^{-\frac{1}{2}} \right], \quad (18)$$

where $n_{geo} = C_{geo} V / (eA)$ is the charge density one would obtain by only considering the geometric capacitance, and $n_{kin} = (\pi/2) [C_{geo} \hbar v_F / (e^2 A)]^2$ is the term that arises due to the consideration of the kinetic capacitance. By integrating Eq. (18), we obtain the charge density $[n = Q / (eA)]$ as a function of voltage V :

$$n = \int_0^V \frac{C dV'}{eA} = n_{geo} - 4n_{kin} \left[-1 + \left(1 + \frac{1}{2} \frac{n_{geo}}{n_{kin}} \right)^{\frac{1}{2}} \right]. \quad (19)$$

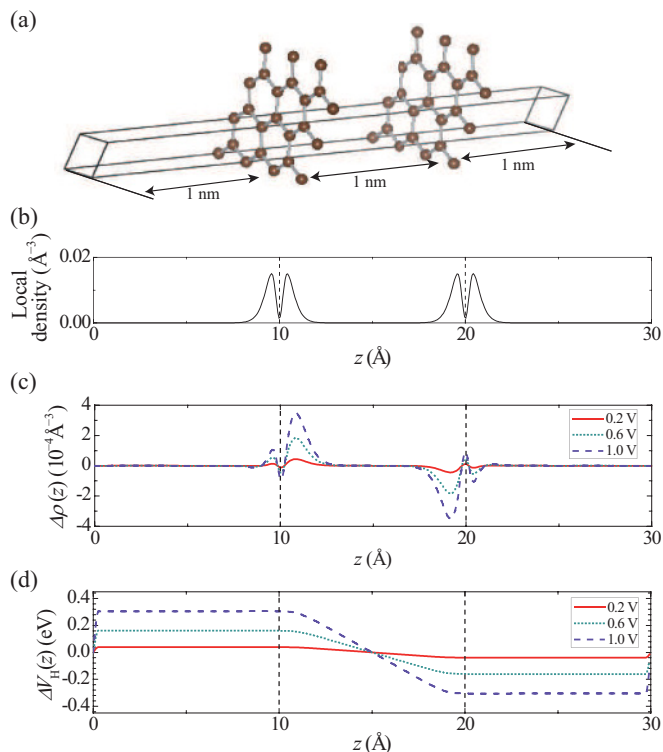


FIG. 10. (Color online) (a) Schematic of the graphene-vacuum-graphene capacitor, (b) xy -plane average of the electron density obtained by integrating the states between ± 1 eV around the Fermi level under zero bias, (c) xy -plane average of the induced charge density at various values of applied bias, and (d) xy -plane average of the electrostatic potential difference with respect to zero bias. The dashed vertical lines correspond to the position of the graphene sheets.

Let us see how well this can describe our results. Figure 10(a) shows the schematic of our model system (two graphene sheets placed 1 nm apart). Since a very accurate Fermi surface is necessary for evaluating the quantum capacitance, we employed a rather dense 161×161 k -point mesh for these calculations. The local electron density around the Fermi level [Fig. 10(b)] is zero at the position of the graphene sheet reflecting the π character of the KS orbitals. The induced charge density profile in Fig. 10(c) has two maxima, which is also related to the π character. The electrostatic potential in Fig. 10(d) does not correspond to the applied bias voltage unlike the previous examples. For example, for $V = 1.0$ V, the electrostatic potential difference between the two graphene sheets is 0.61 eV. This means that the quantum capacitance has a big impact on the total capacitance in this system. Figure 11(a) shows the accumulated charge and the energy increase as a function of bias voltage. We fitted the result to Eq. (19) for $V \geq 0.4$ V and obtained the Fermi velocity of $v_F = 0.77 \times 10^8$ cm/s. This is in fairly good agreement with that evaluated from the linear band structure within 0.1 eV from the Fermi level (0.85×10^8 cm/s). We also obtained a value of 10.8 fF/ μm^2 for C_{geo}/A . This corresponds to an effective vacuum thickness of 0.82 nm. In comparison to the Au-vacuum-Au capacitor examined earlier, the effective surface is closer to the graphene sheet ($\Delta/2 = 0.9$ Å in

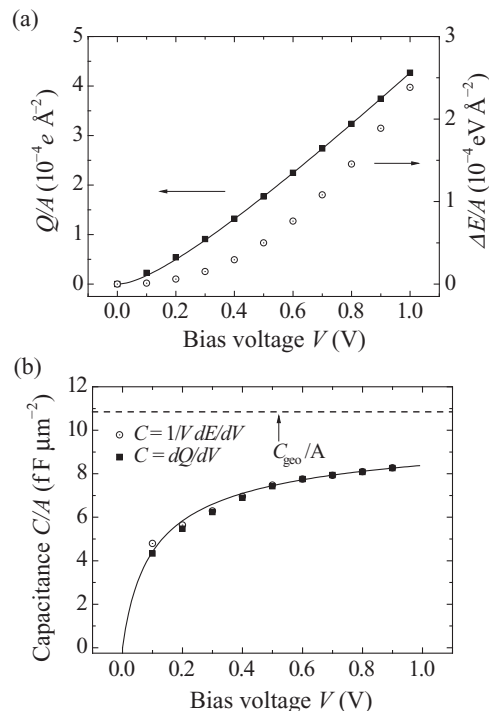


FIG. 11. (a) The accumulated charge of the graphene-1 nm vacuum-graphene capacitor (black squares) and total-energy change (white circles) as a function of bias voltage. (b) The capacitance calculated from voltage vs energy (white circles) and voltage vs induced charge (black squares). The dashed line indicates the geometric capacitance obtained from the V - Q curve.

comparison to $\Delta/2 = 1.5$ Å for Au). This can be explained by the field penetration into the electrodes, as well as the smaller atomic radius of carbon. In Fig. 11(b), we plot the total capacitance evaluated using the charge Eq. (11) and the energy Eq. (12) as a function of bias voltage. The two evaluation methods yield virtually the same results above $V = 0.3$ V (differences are less than 0.7%). The deviation at low voltages can be at least partially attributed to the small changes in the induced charge and energy with respect to bias voltage; smaller values make the numerical evaluation of derivatives using finite differences prone to more noise. The solid curve in Fig. 11(b) is obtained from Eq. (18) based on the parameters extracted from the fit to the V - q curve mentioned above ($v_F = 0.77 \times 10^8$ cm/s, $C_{\text{geo}}/A = 10.8$ fF/ μm^2). It is seen that the numerical results are described well by Eq. (18), which considers the kinetic capacitance. This shows that the OSA captures the quantum effects on the capacitance.

IV. CONCLUSION

In this paper, we proposed an orbital-separation approach (OSA) for simulating the effect of bias voltage within the Kohn-Sham formalism of density-functional theory. The method is robust and efficient, and is readily implemented in existing KS-DFT codes. This approach is unique in that it provides a well-defined total energy of the charged MIM capacitor. Test calculations were performed on Au-vacuum-Au, Au-MgO-Au, and graphene-vacuum-graphene capacitors

to verify the accuracy and reliability of the method. We showed that the capacitance can be calculated from the voltage-energy relation, and that the interface effects on the capacitance can be evaluated by examining the dependence on the dielectric thickness. Both static and optical responses to bias voltage were calculated reliably, testifying to the accuracy of the total energy and the forces obtained using this method. Moreover, we showed that quantum effects on the capacitance can be evaluated as well. Owing to its robustness and efficiency, the OSA holds much future promise for application to a wide range of problems where bias voltage is an important factor including (but not limited to) interfacial capacitance, electrochemical reactions, and scanning probe microscopy.

ACKNOWLEDGMENTS

This work was supported by the Global COE Program “Global Center of Excellence for Mechanical Systems Innovation” and by Asian Core Program by Japan Society for the Promotion of Science (JSPS). It was also supported by Grant-in-Aid for Scientific Research on Innovative Areas, “Materials Design through Computics (2203)” (Grant No. 20104007) and for Scientific Research (B) (Grant No. 20360016) by the Ministry of Education, Culture, Science and Technology (MEXT) of Japan, and Basic Science Research Program through the National Research Foundation of Korea (NRF) funded by the Ministry of Education, Science and Technology of Korea (2010-0011085). S.K. is also supported by Grant-in-Aid for JSPS fellows by MEXT of Japan. The calculations were performed on Hitachi HA8000 cluster system (T2K open supercomputer) at Information Technology Center, the University of Tokyo and SGI Altix 3800EX system at Institute for Solid State Physics, the University of Tokyo. Figures 2(a), 5(a), 8(a), and 10(a) were created using VESTA visualization software (Ref. 39).

APPENDIX: NUMERICAL CRITERIA FOR SEPARATING KS ORBITALS

As mentioned above, a thick enough insulator ensures that the KS orbitals near the Fermi level are well separated into two electrodes. However, KS orbitals are never *exactly* zero anywhere in space. Thus, we need to employ numerical criteria to judge whether each KS orbital belongs to the left or right electrode.

The numerical criteria that we use are as follows: we separate the unit cell of the MIM system into three parts, left (L), center (C), and right (R), where each part roughly coincides with the left electrode + vacuum, insulator, and right electrode + vacuum, respectively (the central part can be thinner than the actual insulator slab to account for metal-induced gap states). We assign the normalized KS orbital ψ_i to the left (right) electrode if

$$\int_{L(R)} |\psi_i|^2 d^3\mathbf{r} > 0.75 \quad (\text{A1})$$

and

$$\int_{L(R)+C} |\psi_i|^2 d^3\mathbf{r} > 0.99. \quad (\text{A2})$$

The first criterion ensures that the orbital originates mostly from the left (right) electrode and not from the insulator or the right (left) electrode. The second criterion accounts for some penetration of the orbital into the insulator. In practice, we sometimes impose a much less strict criterion during self-consistent iterations, as non-self-consistent orbitals are not always well separated into each electrode; in the most extreme case, we can assign ψ_i to the left (right) electrode if

$$\int_{L(R)} |\psi_i|^2 d^3\mathbf{r} > \int_{R(L)} |\psi_i|^2 d^3\mathbf{r}. \quad (\text{A3})$$

In this case, we monitor how well the KS orbitals are separated during self-consistent iterations using the criteria of Eqs. (A1) and (A2) (or possibly even stricter ones). Although the separation may not be ideal at the beginning, it improves as the calculation progresses. The criteria of Eqs. (A1) and (A2) were met at the end of the self-consistent iterations for all of the examples described in this paper. Also, we did not face difficulties due to degeneracy when we started from the ground-state electron density under a small external field as mentioned in the main text. This is because the eigenenergy spectrum for each \mathbf{k} point is rather discrete, so there is very little chance of accidental degeneracy between the electrodes when the charge distribution is asymmetric. However, if we use high densities of \mathbf{k} points or huge unit cells where the eigenenergy spectrum for each \mathbf{k} point is nearly continuous, some accidental degeneracy may occur that could pose problems. In such cases, one may perform a unitary transformation to separate the orbitals.

*kasamatsu@cello.t.u-tokyo.ac.jp

†hansw@snu.ac.kr

¹C. S. Hwang, *J. Appl. Phys.* **92**, 432 (2002).

²D. S. Boesch, J. Son, J. M. LeBeau, J. Cagnon, and S. Stemmer, *Appl. Phys. Express* **1**, 091602 (2008).

³S. K. Kim, S. W. Lee, J. H. Han, B. Lee, S. Han, and C. S. Hwang, *Adv. Funct. Mater.* **20**, 2989 (2010).

⁴T. Kopp and J. Mannhart, *J. Appl. Phys.* **106**, 064504 (2009).

⁵K. Uchida, S. Okada, K. Shiraiishi, and A. Oshiyama, *Phys. Rev. B* **76**, 155436 (2007).

⁶S. Ilani, L. A. K. Donev, M. Kindermann, and P. L. McEuen, *Nat. Phys.* **2**, 687 (2006).

⁷T. Fang, A. Konar, H. Xing, and D. Jena, *Appl. Phys. Lett.* **91**, 092109 (2007).

⁸J. Xia, F. Chen, J. Li, and N. Tao, *Nat. Nanotechnol.* **4**, 505 (2009).

⁹P. Hohenberg and W. Kohn, *Phys. Rev.* **136**, B864 (1964).

¹⁰W. Kohn and L. J. Sham, *Phys. Rev.* **140**, A1133 (1965).

¹¹J. Neugebauer and M. Scheffler, *Phys. Rev. B* **46**, 16067 (1992).

¹²L. Bengtsson, *Phys. Rev. B* **59**, 12301 (1999).

¹³Y. Gohda, Y. Nakamura, K. Watanabe, and S. Watanabe, *Phys. Rev. Lett.* **85**, 1750 (2000).

¹⁴S. Furuya, Y. Gohda, N. Sasaki, and S. Watanabe, *Jpn. J. Appl. Phys.* **41**, L989 (2002).

- ¹⁵N. Nakaoka, K. Tada, S. Watanabe, H. Fujita, and K. Watanabe, *Phys. Rev. Lett.* **86**, 540 (2001).
- ¹⁶M. Brandbyge, J.-L. Mozos, P. Ordejón, J. Taylor, and K. Stokbro, *Phys. Rev. B* **65**, 165401 (2002).
- ¹⁷K. Burke, R. Car, and R. Gebauer, *Phys. Rev. Lett.* **94**, 146803 (2005).
- ¹⁸M. Otani and O. Sugino, *Phys. Rev. B* **73**, 115407 (2006).
- ¹⁹K. Uchida, H. Kageshima, and H. Inokawa, *Phys. Rev. B* **74**, 035408 (2006).
- ²⁰M. Stengel and N. A. Spaldin, *Phys. Rev. B* **75**, 205121 (2007).
- ²¹B. Lee, C.-K. Lee, S. Han, J. Lee, and C. S. Hwang, *J. Appl. Phys.* **103**, 24106 (2008).
- ²²M. Tanaka, Y. Gohda, S. Furuya, and S. Watanabe, *Jpn. J. Appl. Phys.* **42**, L766 (2003).
- ²³B. Lee, S. Han, and J. Lee, *J. Korean Phys. Soc.* **52**, 70 (2008).
- ²⁴M. Stengel, N. A. Spaldin, and D. Vanderbilt, *Nat. Phys.* **5**, 304 (2009).
- ²⁵M. Stengel and N. A. Spaldin, *Nature (London)* **443**, 679 (2006).
- ²⁶M. Stengel, D. Vanderbilt, and N. A. Spaldin, *Nat. Mater.* **8**, 392 (2009).
- ²⁷M. Weinert and J. W. Davenport, *Phys. Rev. B* **45**, 13709 (1992).
- ²⁸R. O. Jones and O. Gunnarsson, *Rev. Mod. Phys.* **61**, 689 (1989).
- ²⁹A. Hellman, B. Razaznejad, and B. I. Lundqvist, *J. Chem. Phys.* **120**, 4593 (2004).
- ³⁰A. Görling, *Phys. Rev. A* **59**, 3359 (1999).
- ³¹J. F. Janak, *Phys. Rev. B* **18**, 7165 (1978).
- ³²S. Goedecker and K. Maschke, *Phys. Rev. B* **45**, 1597 (1992).
- ³³G. Kresse and J. Furthmüller, *Phys. Rev. B* **54**, 11169 (1996).
- ³⁴G. Kresse and J. Furthmüller, *Comput. Mater. Sci.* **6**, 15 (1996).
- ³⁵P. E. Blöchl, *Phys. Rev. B* **50**, 17953 (1994).
- ³⁶G. Kresse and D. Joubert, *Phys. Rev. B* **59**, 1758 (1999).
- ³⁷D. M. Ceperley and B. J. Alder, *Phys. Rev. Lett.* **45**, 566 (1980).
- ³⁸J. P. Perdew and A. Zunger, *Phys. Rev. B* **23**, 5048 (1981).
- ³⁹K. Momma and F. Izumi, *J. Appl. Crystallogr.* **41**, 653 (2008).